Fuel 255 (2019) 115766

Contents lists available at ScienceDirect

Fuel

journal homepage: www.elsevier.com/locate/fuel

Full Length Article

Experimental investigation of pilot-fuel combustion in dual-fuel engines, Part 2: Understanding the underlying mechanisms by means of optical diagnostics

Aleš Srna[a,*], Beat von Rotz[a], Michele Bolla[b], Yuri M. Wright[b,c], Kai Herrmann[d], Konstantinos Boulouchos[b], Gilles Bruneaux[e]

[a] Paul Scherrer Institute, Energy and Environment Division, Forschungstrasse 111, CH-5232 Villigen PSI, Switzerland
[b] ETH Zürich, Institute for Energy Technology, Laboratory for Aerothermochemistry and Combustion Systems, Sonneggstrasse 3, CH-8092 Zürich, Switzerland
[c] Combustion & Flow Solutions GmbH, Switzerland
[d] University of Applied Sciences and Arts Northwestern Switzerland, Institute of Thermal and Fluid Engineering, School of Engineering, Klosterzelgstrasse 2, CH-5210 Windisch, Switzerland
[e] Institut Carnot IFPEN Transports Energie, IFP Energies nouvelles, 1 et 4 avenue de Bois Préau, 92852 Rueil-Malmaison, France

ARTICLE INFO

Keywords:
Dual-fuel combustion
Natural-gas engines
Combustion mode transition
Autoignition
High-speed CH_2O-PLIF
Optical diagnostics

ABSTRACT

The pilot-fuel auto-ignition and combustion under engine-like conditions in compressed methane/air mixtures are investigated in a RCEM using a single-hole coaxial injector. In Part 1, the phenomenology of the pilot-fuel combustion was studied based on the thermodynamic analysis. With the addition of methane, a prolonged pilot-fuel combustion duration was observed, especially at increased EGR rates. The aim of Part 2 is to improve the understanding of the underlying processes governing the pilot-fuel burning and premixed flame initiation in dual-fuel engines. The thermodynamic analysis is supplemented by optical diagnostics including the high-speed CH_2O-PLIF, Schlieren and OH*, and corroborated with homogeneous reactor and laminar flame speed calculations. The investigations focus on determining the role of (a) ignition location and number of ignition kernels, (b) stratification of the autoignition time due to the methane chemistry effects, and (c) the role of flame propagation during the pilot-fuel burning. In the initial phase, combustion is found to propagate through an auto-igniting front. When combustion reaches the lean zones with a high spatial stratification of the autoignition time, premixed flame propagation becomes the dominant mechanism, owing to its higher spreading rate. Both processes influence the pilot-fuel combustion duration. At higher methane concentration, the simulations predict an increasing stratification of the ignition delay in lean regions, while the laminar flame speed in the pilot-fuel lean regions moderately increases. Overall, this explains the observed trend of longer pilot-fuel combustion duration in the dual-fuel cases and indicates an increasing role of flame-propagation in the dual-fuel combustion pilot-fuel burning.

1. Introduction

Lean-premixed pilot-fuel ignited natural gas engines are seen as an attractive solution to fulfill the present and future emission legislation at uncompromised efficiency and lower fuel specific CO_2 emissions. Despite the proven benefits at medium and high loads, a clear emissions/efficiency tradeoff was discovered at low loads – large pilot-fuel portions lead to high emissions of soot and NO_x while reducing the pilot-fuel portion yields to a penalty in the engine efficiency and high unburnt hydrocarbons emissions (UHC) [1–6]. Usually, the dual-fuel engines are engineered by modifications of their diesel/gasoline counterparts. Therefore, it can be assumed that by further development of

Abbreviations: [O_2], Charge oxygen concentration [vol %]; BDC, Bottom Dead Center; CFD, Computational Fluid Dynamics; EGR, Exhaust Gas Recirculation; EOI, End of Injection; ET, Injector Energizing Time; ϕ, Equivalence ratio; ϕ_{C12H26}, Dodecane in air equivalence ratio; ϕ_{CH4}, Charge methane equivalence ratio; FHWM, Full-Width at Half-Maximum; HR, Homogeneous Reactor; HRR, Heat Release Rate; ID, Ignition Delay; NO_x, Nitrogen oxides; OH*, Chemically excited hydroxyl radical; PAH, Poly-Aromatic Hydrocarbons; p_{inj}, Injection pressure; PLIF, Planar Laser-Induced Fluorescence; RCEM, Rapid Compression-Expansion Machine; SOI, Hydraulic Start of Injection; TDC, Top Dead Center; T_{SOI}, Charge temperature at SOI; t_v, Pilot-fuel combustion duration metric; UHC, Unburnt HydroCarbons; UV, Ultra-Violet

* Corresponding author.
E-mail address: a.srna@unsw.edu.au (A. Srna).

https://doi.org/10.1016/j.fuel.2019.115766
Received 19 November 2018; Received in revised form 17 May 2019; Accepted 3 July 2019
Available online 13 July 2019
0016-2361/

the engine geometry and control systems, considerable improvements in efficiency and emission levels can be achieved. This unused potential motivated several dual-fuel combustion engine experiments and optical investigations, e.g. [2,4–12].

Generally, it is understood that methane has a strong inhibiting effect on the pilot-fuel autoignition. With the addition of methane into the air charge at otherwise unchanged conditions, prolonged ignition delays were observed for several technical and surrogate fuels [9,10,13–15]. A recent study by the authors [14] revealed that this influence originates from methane reducing the pilot-fuel reactivity during the cool-flame pilot-fuel autoignition, leading to a delayed onset of the cool-flame ignition in lean pilot-fuel regions. Through the turbulence-chemistry interaction, this influence is propagated to the fuel-rich regions and leads to a delayed high-temperature ignition [14,16]. This interaction can ultimately lead to misfire as well as adverse effects on the cyclic variability, engine efficiency, and UHC emissions [2,4,7,17–19].

While studies on the influence of methane on ignition are established in the literature and the effect understood to a certain extent, considerably fewer investigations studied the impact of methane on the combustion transition phase from autoignition into premixed flame propagation. In this time, the pilot-fuel is being consumed in high-temperature reactions while the in-cylinder flow-field is still dominated by the momentum induced by the pilot spray. However, the conventional engine test-rigs feature very turbulent charge conditions and therefore, the rapid premixed fuel combustion masks the pilot-fuel heat release rate (HRR) [20], making assumptions on the pilot-fuel burning period challenging. Usually, lower pressure rise rates and a longer combustion duration were observed in dual-fuel operation relative to the equivalent diesel mode [3]. Nevertheless, tracking the in-cylinder consumption of pilot-fuel under such turbulent conditions would require a highly advanced set of optical diagnostics. To the authors' best knowledge, no such studies are reported in the literature.

The pilot-fuel burning phase has a paramount influence on the combustion of premixed fuel. The timing, size, and evolution of the initiated flame kernels strongly influence the flame front evolution and were shown to influence the UHC emissions as well as efficiency [4,17–19,21]. In other combustion concepts like RCCI and partially premixed combustion studies, similarly, the pilot-fuel injection strategy was shown to be the main parameter governing the engine efficiency and HRR [22–24]. Generally, the pilot-fuel combustion is understood as a competition between the sequential autoignition and premixed flame propagation [25–27]. The resulting flame kernels were observed to be conical at low injection pressure, while a higher injection pressure leads to a toroidal flame front [11]. For accurate HRR predictions, both the 0D/1D as well as CFD models have to be able to reproduce such characteristics. Many dual-fuel CFD models switch between an autoignition and a flame-propagation model, using different approaches to distinguish when a premixed flame has been established and to switch the model accordingly [27,28]. Furthermore, the 0D-models rely on different assumptions when to change the HRR phenomenological model, for example by assuming conical ignition kernels and the pilot-fuel combustion duration to be proportional to the ignition delay [20].

This study aims to shed light on the underlying processes governing the transition from pilot-fuel ignition to premixed flame propagation in dual-fuel engines. An optically accessible RCEM featuring quiescent conditions was used. In Part 1 of this work [54], the first-order influences of the charge and pilot-injection parameters on the pilot-fuel burning phase were identified based on the HRR analysis. Premixed methane was found to increase the pilot-fuel combustion duration, nevertheless, under some conditions, this pilot-fuel combustion duration was found strongly decoupled from the ignition delay. In Part 2, we corroborate these findings with high-fidelity optical diagnostics to (a) improve the understanding of the underlying fundamental processes governing the combustion and (b) to confirm the conclusions of the HRR analysis. In particular, the interaction between the following processes/effects with regard to the transition time is investigated: (a) the importance of autoignition chemistry during the pilot-fuel combustion, (b) the role of flame propagation during the pilot-fuel burning, and (c) the contribution of the number and distribution of the ignition kernels. High-speed CH_2O-PLIF at 10 kHz was used to trace the persistence of pilot-fuel cool-flame combustion products, complemented by high-speed Schlieren and OH* chemiluminescence imaging at a higher frame rate (80 and 40 kHz, respectively) to trace the appearance of ignition kernels and the spreading rate of burnt zones.

The publication is structured as follows: First, the optical diagnostic setup is introduced. The results section presents the pilot-fuel combustion single-event visualizations in diesel and dual-fuel cases for a variation of pilot-injection strategy. Both CH_2O-PLIF and OH* chemiluminescence results are presented. The evaluation of these results is supported by the homogeneous reactor and laminar flame-speed calculations in order to investigate the methane influence on the propagation speeds of competing combustion modes. Through the discussion, the conclusions on the importance of governing processes during the pilot-fuel burning in dual-fuel engines are drawn.

2. Experimental setup

The experimental apparatus used in Part 2 of this study is the same as described in detail in Part 1 [54] and the references within. Therefore, only a summary is offered here. Experiments are performed in an optically accessible Rapid Compression Expansion Machine (RCEM) with bore of 84 mm and BDC displacement of 1.38 dm^3 (249 mm stroke clearance). Pilot-fuel (*n*-dodecane, 99.4% pure) is admitted into a compressed methane/air mixture using a side-mounted 100 µm single-hole coaxial diesel injector. The methane/air charge with pressure of 1.2 bar is conditioned directly in the combustion chamber by injection of methane into air. After about 4 s time to allow for mixing of methane with air (mixture homogeneity better than 6% [13]), the rapid compression is initiated. When pressure in the cylinder reaches the set threshold (pressure at SOI, p_{SOI}), pilot injection is triggered. Charge conditions in the RCEM are quiescent throughout the cycle (assessed by using PIV [29]). Optical access into the RCEM combustion chamber is offered through two Ø52 mm windows along the cylinder axis as well as through the Ø36 mm side-window used for illumination with a laser-sheet.

Experiments are performed at p_{SOI} of 25 bar. Experimental matrix includes the following variations: temperature at the SOI (T_{SOI}, 770–850 K), methane equivalence ratio (ϕ_{CH4}, range 0–0.66), charge oxygen content ([O_2]) as well as pilot injector energizing time (ET, 300–500 µs) and injection pressure (p_{inj}, 600–1000 bar). Table 1 summarizes the experimental matrix of this study. In Part 1, we were focusing on the combustion heat release rate (HRR) analysis complemented with the non-reactive quantitative optical investigations of pilot-fuel mixing by application of tracer-PLIF, Schlieren, and Mie-scattering. In Part 2, the HRR analysis is complemented with the optical imaging of CH_2O (CH_2O-PLIF), Schlieren and OH* chemiluminescence under reactive conditions.

2.1. CH_2O-PLIF, Schlieren and OH* chemiluminescence optical setup

A simultaneous high-speed imaging of CH_2O-PLIF, Schlieren, and hydroxyl chemiluminescence (OH*) is employed along the same optical axis to simultaneously temporally resolve the consumption of low-temperature combustion products (CH_2O-PLIF) as well as to detect the high-temperature ignition and flame-kernels spreading (Schlieren and OH*). The optical arrangement at the RCEM is shown in Fig. 1.

The Schlieren beam passed the combustion chamber along the cylinder axis. The same Schlieren setup and settings as used for the non-reactive measurements (Part 1, [54]) was used here as well. Schlieren imaging frame-rate is 80 kHz and resolution 0.18 mm/pixel. A pulsed laser diode (690 nm, Cavitar Cavilux Smart) is used as the light source.

Table 1
Overview of the operating conditions. Values in the 2nd row relate to the variation of T_{SOI} and ET, values in the 3rd row describe the variation of the P_{inj}, and values in the 4th row show the EGR cases (reduced oxygen content). The parameters varied in each column are printed bold.

	T_{SOI}/ET variation	P_{inj} variation	EGR variation [O_2]
BDC displacement		1.38 dm^3	
Charge intake pressure		1.2 bar	
Stroke		236.5 mm ± 1 mm	
Compression ratio		20	
Pressure at SOI (P_{SOI})		25 bar	
BDC temperature	343, 363, 383 K		363, 383 K
Temperature at SOI (T_{SOI})	775, 810, 850 K		810, 850 K
Pilot injector energizing time (ET)	**300, 400, 500 µs**	300 µs	400 µs
Pilot injection duration	**0.40, 0.58, 0.77 ms**	0.45 ms	0.58 ms
Pilot injection pressure	600 bar	**1000 bar**	600 bar
Injected pilot-fuel mass [mg]	**0.64, 1.18, 1.81 mg**	1.21 mg	1.18 mg
Charge oxygen content % [O_2]	21	21	**18, 15**
Methane/air mixture equivalence ratio (φ_{CH4})	0, 0.33, 0.48, 0.53, 0.58, 0.66	0, 0.48, 0.53, 0.58	18% [O_2]: 0, 0.56, 0.62, 0.68 15% [O_2]: 0, 0.67, 0.74, 0.81
CH_4 injected mass	0–64 mg	0–56 mg	0–56 mg

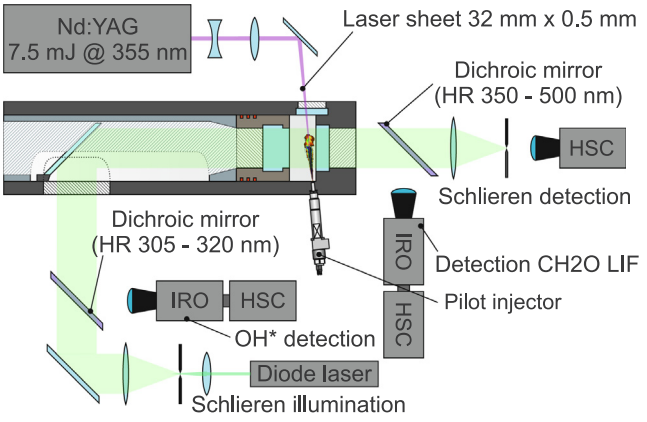

Fig. 1. Optical setup for simultaneous high-speed schlieren, CH_2O-PLIF and OH* chemiluminescence imaging at RCEM [14].

Dichroic mirrors are used to separate the short-wavelength CH_2O-PLIF and OH* signal from the Schlieren beam, therefore, enabling imaging with the three methods along the same optical axis. All devices are synchronized to the electronic start of injection trigger using a LaVision timing unit.

2.1.1. CH_2O-PLIF

The formaldehyde fluorescence is excited using the 3rd harmonic output of a high-speed diode-pumped Q-switched Nd:YAG laser (Edgewave IS400, 7.5 mJ/pulse at 355 nm, 10 kHz repetition rate). A laser sheet with height of 50 mm and about 1 mm thickness is formed using a combination of cylindrical and spherical lenses. The central 32 mm of the laser-sheet are directed towards the injector orifice under an angle of 3.5° relative to the plane of the cylinder head surface. On the detection side, radiation in the wavelength range of 350–500 nm is separated from the Schlieren beam at a dichroic beamsplitter plate (Newport 66238). The bandpass filtered PLIF signal (400–480 nm, Chroma technology) is collected with a Nikkor 105 mm f/2.8 glass lens and detected with an image intensifier (LaVision HS-IRO) coupled to a high-speed camera (Photron Fastcam SA1.1). The projected pixel size is 0.11 mm/pixel. The intensifier gate is set to 100 ns and the gain to 37 counts/photoelectron. Image flat-field correction is performed by the tracer-PLIF images of homogeneously seeded TMPD[1] vapor in a nitrogen atmosphere, which was introduced into the combustion chamber of the RCEM. No measures had to be undertaken to avoid the off-plane PLIF signal interference due to the laser-light reflections on metallic chamber walls – the tests with homogeneously seeded TMPD vapor and structured light-sheet illumination showed no indication of a such interference. The pulse energy fluctuations are monitored by measuring the intensity of the sampled laser beam using a fast photodiode and SRS Boxcar integrator.

During the auto-ignition process, the moving piston compresses the fuel cloud towards the cylinder head. This motivates the 3.5° angle of the laser-sheet plane instead of a plane along the injector axis (5° inclination). In a pre-study (unpublished), two high-speed intensified cameras detecting OH* chemiluminescence simultaneously through the main and the side window were used to determine the axial and radial position of the ignition spot. This optimal laser-sheet inclination of 3.5° was selected based on a best-fit through the ignition spots under different conditions.

The detection of CH_2O by 355 nm-PLIF excitation in sooting diesel sprays is known to suffer from interference by the polyaromatic hydrocarbons (PAH) [30,31] and laser-induced incandescence (LII) [32]. Only a small portion of the investigated conditions in this study produces soot [33]. In this cases, the PAH interference is distinguished from the CH_2O-PLIF based on the differences in the relative intensity [34] and the spatial and temporal criterion [31,32,35].

2.1.2. OH* chemiluminescence

Filtered flame emission in the spectral range of chemically excited hydroxyl (OH*) is acquired using a second intensified high-speed camera (Photron FastCam SA1.1 with LaVision HS-IRO) at a frame rate of 40 kHz. The intensifier is equipped with an UV lens (Sodern Cerco 100 mm f/2.8) and bandpass filter (313 nm ± 13 nm). The resulting resolution is 0.18 mm/pixel. Intensifier gate is set to 20 µs, and the gain adapted to the brightness of flame emission under different conditions (9–45 counts/photoelectron). A higher intensifier gain is necessary in the reduced [O_2] cases due to a significant decrease in OH* emission. The gain setting of up to 190 counts/photoelectron is used to achieve the best-possible signal-to-noise ratio. The UV radiation is separated from the Schlieren beam using a 308 nm 45° laser mirror (100 mm diameter).

2.2. Imaging results and processing

An exemplary image-series of a dual-fuel combustion event is presented in Fig. 2. Images from all three optical methods are presented down-sampled to the 10 kHz frame-rate of CH_2O-PLIF imaging. The intensity scales are given in arbitrary units, where 1 a.u. corresponds to the camera full dynamic range, corrected for the variable gain of the image intensifier. All images in this publication use the same intensity

[1] n,n,n′,n′-tetramethyl-p-phenylene-diamine.

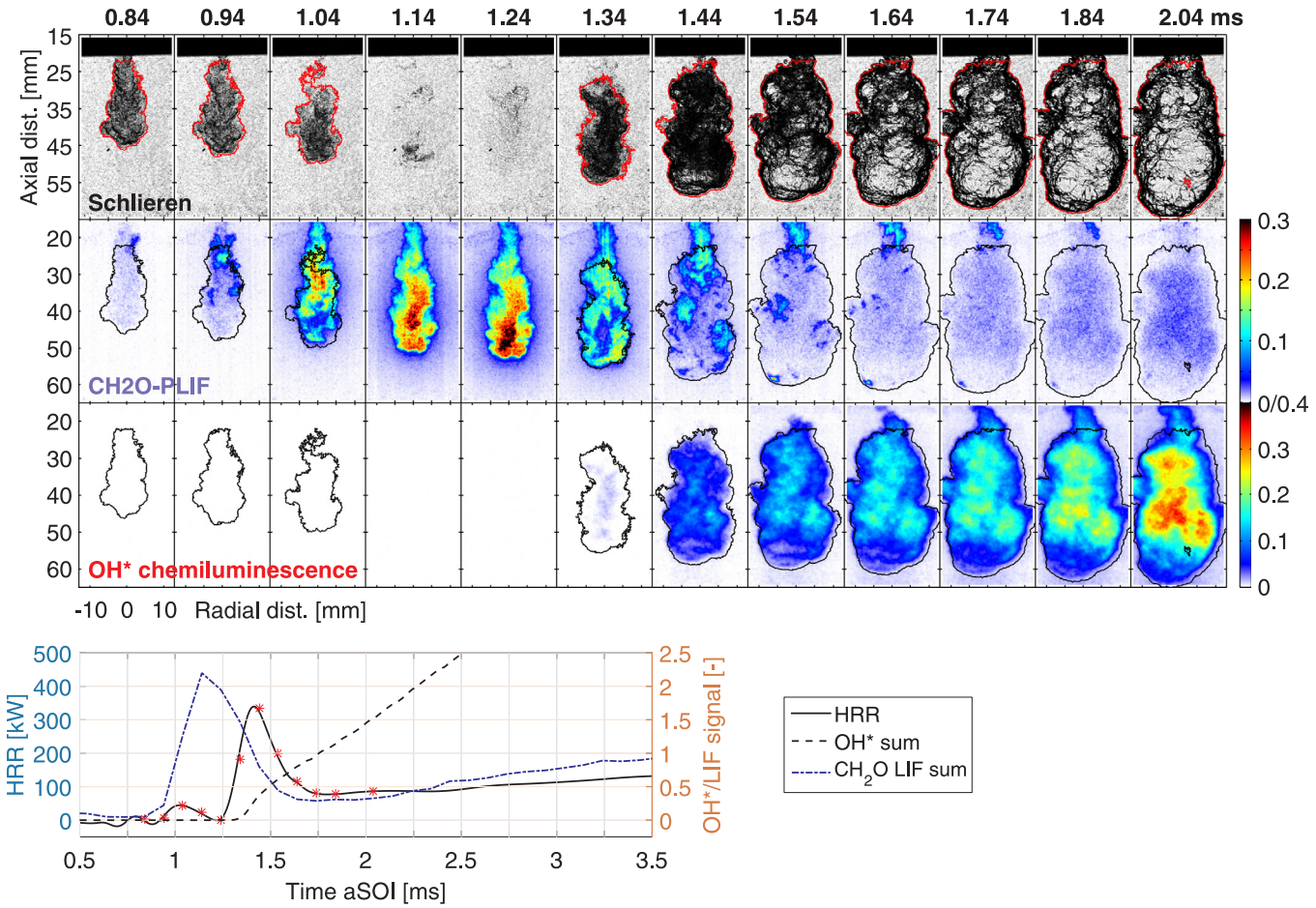

Fig. 2. A series of image panels showing the simultaneously acquired raw images from Schlieren (upper row), CH_2O-PLIF (middle row) and OH* chemiluminescence (bottom row). The same color scale was used for all CH_2O-PLIF panels within this work. Overlaid are the spray contours from processed Schlieren images. Time aSOI is indicated above each column. The bottom plot shows the HRR, total OH* chemiluminescence signal, and total CH_2O-PLIF signal. Asterisk symbols indicate the time instants of the image-panels above. Conditions: T_{SOI} = 810 K, ϕ_{CH4} = 0.59, ET = 400 µs, p_{inj} = 600 bar.

scale, meaning the intensities are directly comparable to each other. The schlieren-images show a two-stage ignition event with low-T reactions before the onset of the high-temperature ignition – first, a contrast-decrease of Schlieren-contours is detected at the spray periphery, as the first CH_2O-PLIF signal appears at 0.84 ms aSOI. The low-T reactions then spread along the spray periphery towards the spray tip and towards the spray axis. At the same time, the Schlieren contrast further reduces, and just before ignition (1.24 ms), barely any Schlieren signal is visible. This disappearance of the Schlieren signal is attributed to the heat-release from the first-stage ignition, compensating for the refractive index change due to the fuel evaporative cooling, as reported before in the diesel [31,36] and in dual-fuel combustion [9,37]. The ignition occurs between the image panels at 1.24 and 1.34 ms and is indicated by the disappearance of a part of the CH_2O-PLIF cloud, the reappearance of the Schlieren signal with high contrast, and the first appearance of the OH* chemiluminescence signal. The ignition kernel then spreads through the pilot-fuel cloud, and the remaining CH_2O is quickly consumed, except close to the injector orifice. At the same time, the Schlieren contour spreads and smoothens as the laminar flame propagation is initiated. Simultaneously, a very high rise of the OH* signal is observed. The analysis of the HRR (Fig. 2, bottom plot) shows a good agreement of the cool-flame and high-temperature peaks of the HRR with the interpretation of optical results. The source of the moderate-intensity signal in CH_2O-PLIF images at late-times after ignition (wide-spread, covering the center of the burnt area) is attributed to the strong CO_2* fluorescence, based on the spectrally resolved flame-emission detection [38] using a similar diagnostic setup as [39].

The optical data is further processed to extract the spray and flame contours, as well as to detect the ignition and the flame-kernels. Schlieren images are processed using the adaptive background subtraction methodology as proposed by the Engine Combustion Network [40]. The processing begins with the first acquired image serving as the background subtracted from the following image. After the background subtraction, the spray/flame regions are separated from the surroundings based on a thresholding approach, and the process continues with assuming the regions without any spray detected as the new background. The previous background is assumed for the regions with the detected spray. This adapted background is then subtracted from the next image. The threshold level was selected in a trial-and-fail procedure until the methodology reliably detected the spray-contour. The qualitative performance of this spray-edge detection routine is demonstrated by the red/black contours in Fig. 2. The automated spray-contour detection just prior to ignition is not reliable and not drawn due to the strongly diminished schlieren signal.

Also the OH* chemiluminescence images were processed using a thresholding approach. Ignition is detected by the OH* signal exceeding a threshold of 40 counts in an area larger than 60 pixel. This threshold relates to the lowest intensifier gain and was selected as the minimal threshold reliably separating ignition cores from the noise. This threshold level was adapted analogously to the higher intensifier gain setting. Furthermore, in the reduced charge [O_2] cases a reduced threshold (20 counts) with a manual verification is necessary to avoid an over-predicted ignition delay due to the considerably weaker OH* signal. The thresholding method is also proposed by the Engine

Combustion Network [41] and found to reliably detect the ignition, though the threshold used within the ECN is much higher (50% maximal intensity) than the threshold used here.

A thresholding technique is also used to determine the evolution of flame-kernels. Nevertheless, the strong scattering of light from the bright central burnt zones was found to raise the signal over the entire window to above the background level before ignition. Therefore, after the ignition was detected, the threshold for flame spreading is adapted based on the highest flame brightness in each frame – 40 counts plus 2% of the maximal detected brightness.

3. Results

The results section first establishes a theoretical background for combustion transition process by simulating the influence of methane on the pilot-fuel autoignition and premixed flame speed. Homogeneous reactor (HR) and laminar flame speed calculations are presented for this purpose. These calculations, despite representing a very simplified view of the combustion process, were employed for predictions of the methane influence on the combustion during the combustion transition process from the first autoignition kernel within the pilot-fuel jet until a premixed flame in the methane/air mixture is fully established. In the second part, the experimental evidence for the calculated influences is seeked by comparing the pilot-fuel consumption and flame spreading of the diesel and dual-fuel combustion events.

3.1. Calculations: methane influence on the auto-ignition front and laminar flame spreading rates

In the RCCI and HCCI combustion processes, an auto-igniting front is often assumed to be the mechanism responsible for combustion propagation through the combustion chamber [24,42]. This mechanism assumes that the diffusion of heat and radicals within the flame front plays a minor role in the spreading of combustion – only the mixture composition and temperature define the time of ignition. The inhomogeneity of mixture or temperature within the combustion chamber leads to a cascade of auto-ignition events, which form an autoignition flame front. The spreading rate of this auto-ignition flame front can be described by the Zeldovich criterion [43] as the inverse gradient of auto-ignition time. Numerical simulations have found signs of autoignition front also in autoigniting diesel [44] and dual-fuel jets [14]. In pilot-fuel jets, the auto-ignition time stratification correlates in the first-order to the mixture spatial stratification, if neglecting the mixing history of different fuel parcels and the turbulence-chemistry interactions [14,44]. Since the injection durations are extremely short for these micro pilot sprays, scalar dissipation rates can be expected to decay rapidly compared to steady jets, while end-of-injection transients additionally promote mixing [45–47]. To estimate the autoignition time sensitivity to mixture composition, homogeneous reactor calculations using Cantera software are employed. The reduced chemical mechanism for dodecane by Ranzi et al. (130 species, 2323 reactions, [48]) is used. This mechanism choice is motivated by the findings of a comprehensive mechanism assessment for methane/dodecane air mixtures reported in [49] and a comparative LES study for auto-igniting dual-fuel sprays in [16]. Additionally, to validate the mechanism choice, the calculations were repeated for a subset of cases using the substantially more complex detailed mechanisms (Polimi [50] and LLNL [51]), yielding qualitatively the same conclusions. Autoignition times for a range of dodecane/methane/air mixtures are calculated and the 80% temperature rise criterion, as proposed in [44], is applied to detect the ignition. Fig. 3a shows the high-temperature ignition delay from HR calculations at $T_{SOI} = 770\,K$ for different pilot-fuel equivalence ratios ϕ_{C12H26} and variation of premixed fuel ϕ_{CH4}. Both equivalence ratios are defined as for mixing of fuel in air as $\phi = \frac{[\text{fuel}]\,/\,[\text{oxidant}]_{air}}{[\text{fuel}]_{st}\,/\,[\text{oxidant}]_{air}}$, even when the charge oxidant concentration is reduced.

The addition of methane shifts the most reactive mixture towards pilot-fuel richer conditions and delays the ignition by about 20% (Fig. 3a). Here, the reactivity is interpreted as the mixture ignitability, correspondingly, the mixtures exhibiting shorter ignition delay and less sensitivity to mixture composition and temperature are considered more reactive. At the pilot-fuel-richer mixture fractions, the influence of methane diminishes. On the other hand, a considerable stratification of the ignition delay is observed in the pilot-lean regions, especially when leaner than $\phi_{C12H26} = 0.5$. Kahila et al. [16] showed that the ambient methane influences the early decomposition of n-dodecane, mainly by consuming OH radical and forming methyl radicals, which activate other inhibiting reactions. This can be further discerned from the methane dilution effect by the dotted line in Fig. 3a: a calculation for $\phi_{CH4} = 0.66$ is performed, however, with methane initiated as an inert species – not participating in chemical reactions but diluting the mixture and changing its thermal capacity (as proposed in [9;14]). An about four-times lower ϕ_{CH4} influence is predicted with the inert methane species, indicating a strong chemical involvement of methane in the lean-mixtures autoignition.

The auto-ignition time gradients in the lean-mixtures considerably increase with the introduction of methane. For example, already at $\phi_{C12H26} = 0.45$, a 45% increase of the ignition delay is predicted. In absolute terms, this increase is three-times higher than the increase of ID in the most reactive mixtures. Therefore, the Zeldovich criterion [43] predicts a considerable decrease of the front propagation speed across the mixture, especially in the cases when very lean pilot-fuel mixtures at ignition are reached. This is in agreement with the prolonged pilot-fuel combustion duration reported in Part 1 of this study.

Fig. 3 b) and c) additionally assess the methane influence on ignition for (b) a variation of T_{SOI} and (c) a variation of $[O_2]$. Only the $\phi_{CH4} = 0$ and 0.60 curves are plotted for clarity. Under all considered charge conditions, a similar chemical influence of CH_4 was calculated, showing a deferred auto-ignition in the lean pilot-fuel mixture and a shift of the most-reactive mixture to fuel-richer conditions. A similar influence is observed when increasing the ϕ_{CH4} in the reduced $[O_2]$ cases. Furthermore, it appears that under reduced $[O_2]$ the influence of methane is moderately amplified, apparent from a larger separation of ignition delay curves in the lean-zones.

The competing mechanism to the autoigniting flame-front is the flame propagation. The major difference from the autoigniting front is that the transport of heat and radicals within the flame front governs the spreading rate. Flame propagation is expected to be the faster mechanism in zones with very high ignition time stratification, e.g., in the dual-fuel cases in the very lean pilot-fuel regions. Within the pilot-fuel jet, the flow conditions are likely to be turbulent. The influence of turbulence on the premixed flame is considerable and many correlations of the ratio of turbulent over laminar flame speed are available [52]. The most basic yet widespread Damkoehler closure assumes a linear relation of the turbulent/laminar flame speed ratio to the turbulence intensity. In the context of this work, when methane is introduced into the charge, the turbulence flow field is expected not to change, however, no information of the actual turbulence intensity is available and simulations in the 3D-CFD context are out of the scope of this study. Based on this reasoning, assuming the Damkoehler closure, the influence of methane on the flame speed is assessed by the laminar flame-speed calculations.

The laminar flame speed (burnt side[2]) is calculated using Cantera software for a range of dodecane/methane/air mixtures (Fig. 4). These calculations use the same chemical mechanism as for the homogeneous reactor calculations [48]. At 21% $[O_2]$ (black), the highest flame speeds among the selected mixtures are predicted for around-stoichiometric

[2] Fresh gas laminar flame speed multiplied by the volume expansion ratio from the change of density over the flame front.

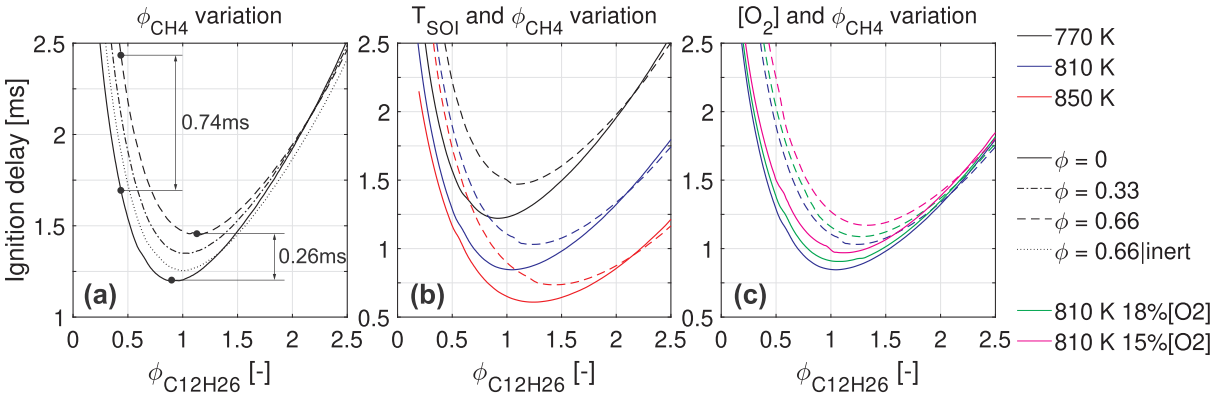

Fig. 3. Homogeneous reactor simulations of the ignition delay dependence on pilot-fuel equivalence ratio for (a) a variation of ϕ_{CH4} at a fixed T_{SOI} = 770 K, (b) variation of T_{SOI} and ϕ_{CH4}, and (c) variation of [O_2] and ϕ_{CH4}. Line color determines the T_{SOI} and [O_2], line-style the ϕ_{CH4}. The dotted line (a) shows the ignition delay dependence, when methane is added to the chemical mechanism as an inert species. The ϕ_{C12H26} describes the equivalence ratio of dodecane related to 21% [O_2], also in the EGR cases (c).

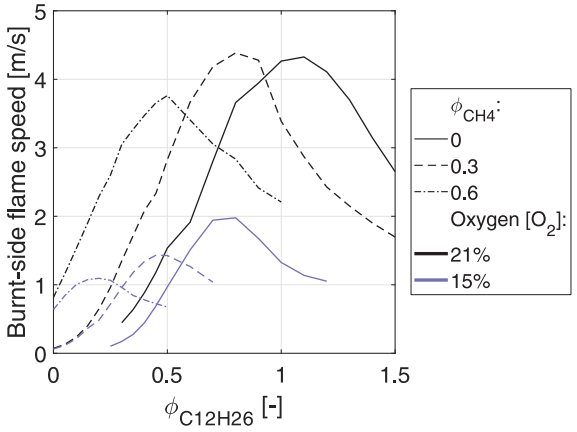

Fig. 4. Dependence of the dodecane/methane/air mixture burnt-side laminar flame speed on ϕ_{C12H26} for a variation of ϕ_{CH4} (line style) and [O_2] (color), T_{SOI} = 850 K.

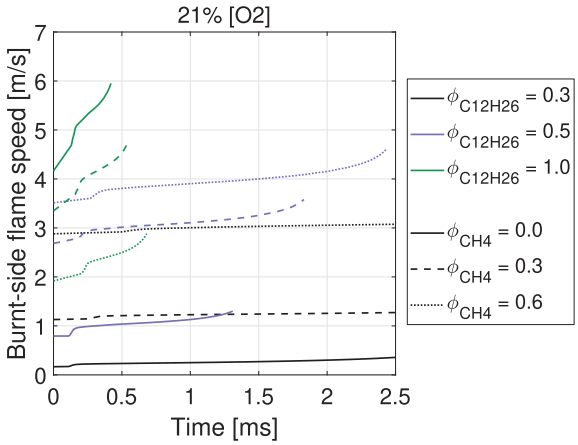

Fig. 5. Temporal evolution of the burnt-side flame speed in mixtures of dodecane/methane/air mixtures at 850 K and 21% [O_2]. Line color determines the ϕ_{C12H26}, line-style the ϕ_{CH4}. The lines are drawn up to the time shortly before ignition.

dodecane mixtures, with the speed ranging up to 4.2 m/s. With the admixture of methane, the peak laminar flame-speed values shift to a leaner pilot-fuel concentration and keep reaching similar values as for the neat air/dodecane mixture. The methane laminar flame speed in neat air at ϕ_{CH4} = 0.6 is about 0.9 m/s. However, with a small addition of dodecane, this increases to around 1.8 m/s at ϕ_{C12H26} = 0.2 and to 3.8 ms at ϕ_{C12H26} = 0.5. On the other hand, the laminar flame speed for neat and lean ϕ_{C12H26} = 0.15–0.5 range between 0.1 and 1 m/s. Not surprisingly, the addition of methane to a lean dodecane/air mixture considerably increases the flame propagation speed.

When reducing the charge oxygen content [O_2] (Fig. 4, blue), much lower flame speeds are predicted due to the reduced flame temperature. At the same fuel concentration, comparable flame-speeds are calculated only for the leanest conditions, where oxygen is abundant. In the fuel-richer zones, the difference in flame speeds for the different oxygen contents becomes substantial, especially with higher ϕ_{CH4}. The combination of reduced [O_2] and high ϕ_{CH4} leads to an overall high equivalence ratio and low flame speed. The maximal flame speed of about 1 m/s at 15% [O_2] reaches only ¼ of the maximal speed in air. This indicates that the flame propagation during the transition process is considerably impaired in the reduced [O_2] cases. Therefore, the role of autoigniting front (ignition time stratification) is more pronounced in these cases.

For the assessment of transition process in an autoigniting spray, the change of the flame speed due to the increase of charge temperature and reactivity due to the autoignition in progress is plotted in Fig. 5.

This is elaborated by tracking the temporal evolution of the burnt-side laminar flame speed for selected combinations of ϕ_{CH4} and ϕ_{C12H26} in air (Fig. 5), analogous to Soriano and Richardson [26]. The temporal evolution of flame speed is captured by first initiating the HR calculation. Every 10 µs, the composition of HR reactor is exported and used as the inlet flow composition of a laminar flame speed calculation. To avoid the convergence problems due to a too reactive input mixture, the simulation is terminated when the temperature in HR exceeds 1050 K.

During the first-stage ignition, the mixture temperature and reactivity increase, resulting in an about 20% higher laminar flame speed for all conditions. Thereafter, the flame speed keeps slowly increasing as the mixture further heats up when approaching ignition. The highest change of the flame speed over time is observed for conditions with the highest dodecane concentration. Nevertheless, the overall temporal dependence of flame speed due to the ongoing autoignition is rather low. This applies especially in leaner mixtures, where the competition of the premixed flame propagation and autoignition is expected. Therefore, already the laminar flame-speed calculation provides a good indication of the expected flame-speed dependency on ϕ_{CH4}.

3.2. Pilot-fuel burning traced by the CH_2O-PLIF imaging

In experiments, the high-speed CH_2O-PLIF imaging enables tracing of the low-T combustion products from the first cool-flame reactions until all pilot-fuel is consumed. Within this section, single repetitions of

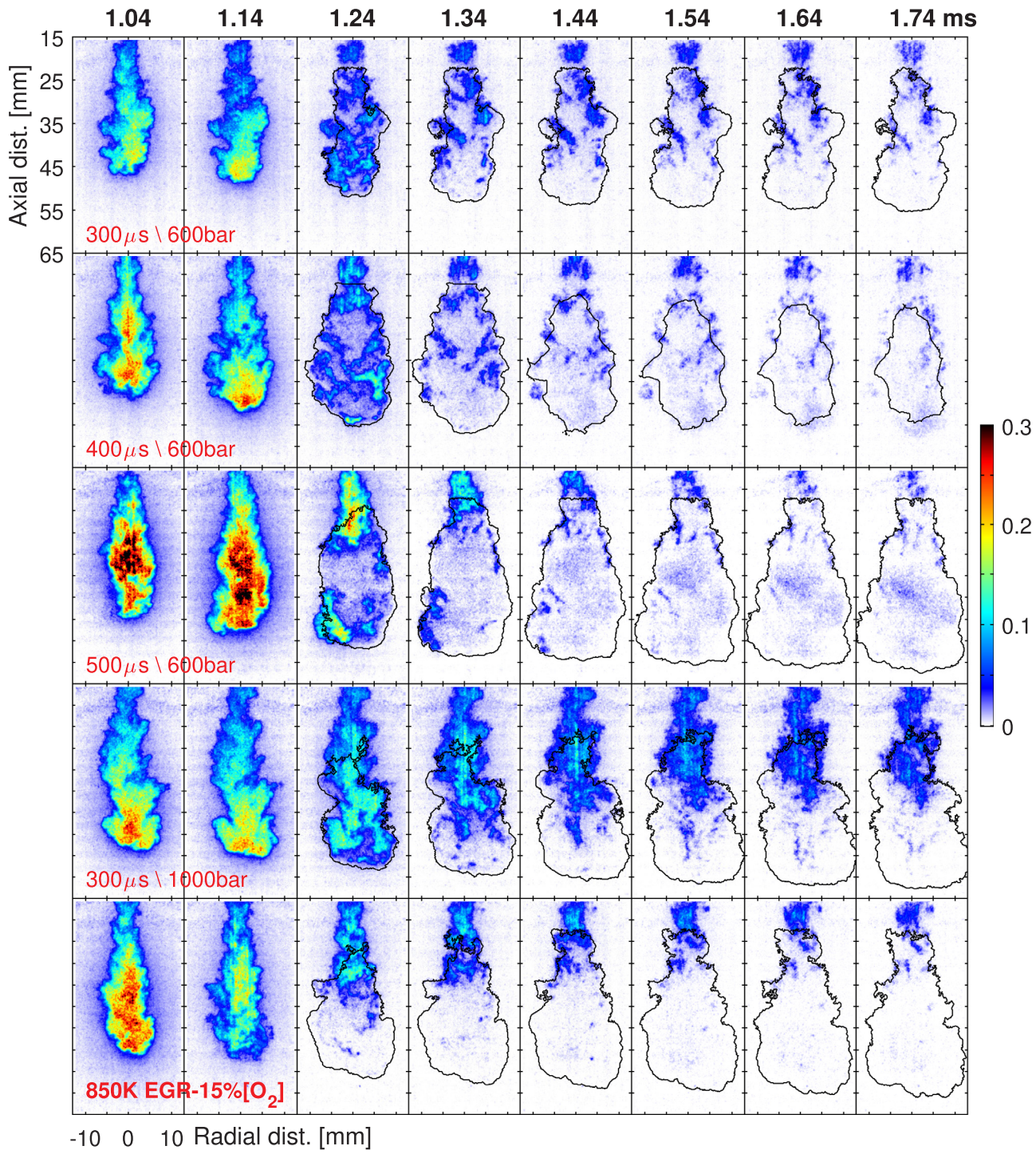

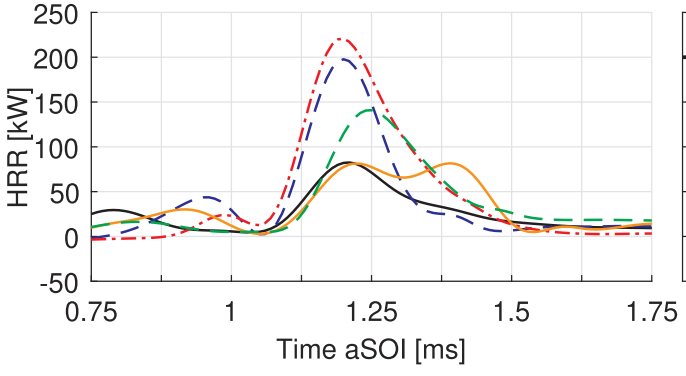

Line Style	Injection	Low-T ID	High-T ID
———	300μs \ 600bar	0.74 ms	1.02 ms
– – –	400μs \ 600bar	0.74 ms	1.07 ms
-·-·-	500μs \ 600bar	0.74 ms	1.10 ms
———	300μs \ 1000bar	0.74 ms	1.07 ms
– – –	850K EGR-15%[O_2]	0.54 ms	1.07 ms

(caption on next page)

Fig. 6. Diesel-case CH_2O-PLIF image time-series for variations of pilot injection parameters: ET variation (rows 1–3), p_{inj} variation (row 4) and $[O_2]$ variation (row 5, ET = 400 μs, p_{inj} = 600 bar). The same color scale was used for all CH_2O-PLIF panels within this work. Simultaneously acquired Schlieren contours are superimposed on panels after the ID (black line). The bottom plot shows the HRR for all five cases, and the table states the low-T and high-T ID. T_{SOI} = 770 K (except 15% $[O_2]$ case, row 5).

the experiment are presented in order to visualize large structures within the spray, which would vanish by ensemble averaging. The presented repetitions were carefully selected by studying all available images to select the most representative experiment. The repeatability of experiments is in generally very high, with the ignition delay standard deviation better than σ = 3% [14].

3.2.1. Diesel cases

Fig. 6 presents the evolution of CH_2O-PLIF signal of single events for a variation of the ET and the injection pressure at T_{SOI} = 770 K. Due to the frame-rate limitation of the CH_2O-PLIF technique, the lowest T_{SOI} conditions have been selected for this comparison so that more relevant frames of a single event can be presented. Additionally, an EGR case (15% $[O_2]$) featuring a similar ignition delay is presented. The first image panel before ignition and the consequent panels until the pilot-fuel is consumed are shown. Before ignition (not-shown), a propagation of the cool-flame occurs (visible on Fig. 6 as a small HRR before the main combustion) similarly as presented on Fig. 2.

The maximal pilot-fuel equivalence ratio of these cases at ignition (cf. Part 1, [54]) varies by about a factor of 2 between 0.8 (ET = 300 μs) and 1.7 (ET = 500 μs). According to the 1D-flamelet simulations by Dahms et al. [44], CH_2O concentration prior to the ignition correlates well with the concentration of pilot/diesel fuel up to $\phi_{C12H26} \approx 5$. Though the fluorescent yield of CH_2O in air at elevated temperature is not well characterized, a low sensitivity of the fluorescence yield to temperature or pressure based on the general fluorescence properties of similar ketone species can be expected [53]. Therefore, within this work a monotonous correlation of the PLIF signal to CH_2O concentration was assumed.

The ET = 300 μs injection results in the leanest conditions at ignition among all considered cases (Fig. 6, upper row). Before ignition, the highest PLIF signal was detected at the spray tip. However, rather than at the spray tip, the ignition as indicated by the first CH_2O consumption[3] is detected in a small region around 30 mm from the injector at 1.14 ms aSOI. Following the first ignition kernel at 1.14 ms, several new ignition zones appear at 1.24 ms aSOI. The remaining CH_2O-PLIF signal is distributed in torn-up zones with apparently lower reactivity and is rapidly consumed. Several very lean unburnt zones close to the injector persist. Such zones are believed to be too lean to autoignite and the primary source of unburnt hydrocarbons in diesel engines [45].

When the injection duration is increased (400 μs/500 μs ET, 2nd/3rd row, Fig. 6), a higher peak CH_2O-PLIF signal is observed as expected considering the fuel-richer conditions. Following ignition, the distribution of remaining CH_2O appeared to be less scattered than in the ET = 300 μs case and limited to the jet periphery. This indicates a volumetric ignition, simultaneously over large zones. Faster consumption of the residual CH_2O both at the jet periphery and close to the injector is observed when increasing the ET. Due to the shorter ignition dwell time, less overmixing is expected to occur near the injector, hence, reducing the very lean zones. In addition, more injection turbulence improves the entrainment of lean mixtures into the hot burnt gases and therefore, faster lean-mixture consumption is favored.

In the high-pressure injection (1000 bar) case, a more intense entrainment wave is expected after the end of injection (EOI) [46]. This is visible by a higher gradient of the CH_2O-PLIF signal from the spray tip towards the injector. Differently than in the p_{inj} = 600 bar cases, ignition occurs at the spray tip on the periphery of the jet and penetrates upstream and towards the spray axis. The considerable persistence of CH_2O late in the cycle implies a significant extent of the lean regions upstream of the spray tip. The prolonged time for a complete pilot-fuel combustion is clearly visible also on the HRR plots (bottom plot, Fig. 6).

Under the reduced $[O_2]$ conditions, the pilot fuel-concentration of the ET = 400 μs case does not change, however, due to a reduced oxygen content, the charge experiences much higher equivalence ratios. The first CH_2O is consumed at the jet periphery with a rather quick consumption of CH_2O at the spray tip. Similar persistence of CH_2O late in the cycle as in the 21% $[O_2]$ 400 μs and 500 μs ET cases (2nd and 3rd row, Fig. 6) is observed. In comparison to the 21% $[O_2]$ case, the HRR curve shows a somewhat slower HRR rise at ignition and a comparably fast drop of the HRR after the peak.

3.2.2. Dual-fuel cases

The variances between the different pilot-injections under the dual-fuel conditions are expected to be larger than in the diesel-cases. This is due to the methane-influence on the lean pilot-fuel mixtures (Fig. 7). The cases with ϕ_{CH4} = 0.59 at 770 K were identified in Part 1 [54] to exhibit a wide range of pilot-fuel combustion duration (0.7–1.4 ms). The shorter injections have longer combustion times and were believed to be close to lean-out – the maximal ϕ_{C12H26} at ignition ranges between 0.4 (short injections) and 1.0 (long injection).

The evolution of CH_2O distribution during the pilot-fuel consumption in the dual-fuel cases is presented on Fig. 7. In the case of a short ET = 300 μs injection (1st row), ignition occurs in the zone with the highest PLIF signal prior to the ignition. A slower rate of PLIF-signal disappearance is visible, and the time needed to reach the peak HRR is doubled relative to the diesel case. Surprisingly though, the persistence of CH_2O late after ignition is comparable to the diesel-case. This is noteworthy since the HR reactor calculations predicted methane to strongly delay autoignition in the pilot-fuel lean zones. Considering the 0.55 ms longer ignition delay relative to the diesel case, the pilot-fuel mixtures at ignition are much leaner than in the diesel case. Therefore, assuming that the persisting CH_2O is located in the zones too lean to autoignite [32], a much higher persistence of CH_2O would be expected. The flame propagation consuming the remaining CH_2O can explain these observations. This conclusion is indirect, since the available experimental methods cannot distinguish a flame propagation from autoignition. Additional support for this conclusion is sought by comparing the CH_2O persistence for different injection strategies and by the additional data evaluation presented in next sections.

Continuing the analysis with the longer 400 and 500 μs ET injections (2nd and 3rd row, Fig. 7), again, ignition first occurs in the regions with the highest PLIF signal before ignition. However, particularly the 500 μs injection shows very distributed persistent CH_2O regions after the ignition. This is comparable to the ET = 300 μs injection in the diesel-case, while no such behavior was not observed in the longer injection diesel cases. Considering a comparable mixing state and ignition dwell time of the ET = 300 μs diesel and the ET = 500 μs dual-fuel case, this is not surprising. Nevertheless, in the lean zones a significantly lower persistence of CH_2O is observed in the dual-fuel case. This, again, indicates a significant role of flame propagation.

The resemblance of the diesel and dual-fuel case of the high-pressure injection (4th row, Fig. 7) is high. The ignition occurs at the spray tip and first spreads around the periphery of the spray tip. The new ignition zones then slowly consume the CH_2O upstream of the spray-head. Again, a similar CH_2O persistence close to the spray tip as in the diesel-case is observed.

Contrary to the 21% $[O_2]$ cases, a very low resemblance of the diesel

[3] This consumption is determined only qualitatively from the high-speed PLIF sequence but agrees well with the first appearance of OH* signal.

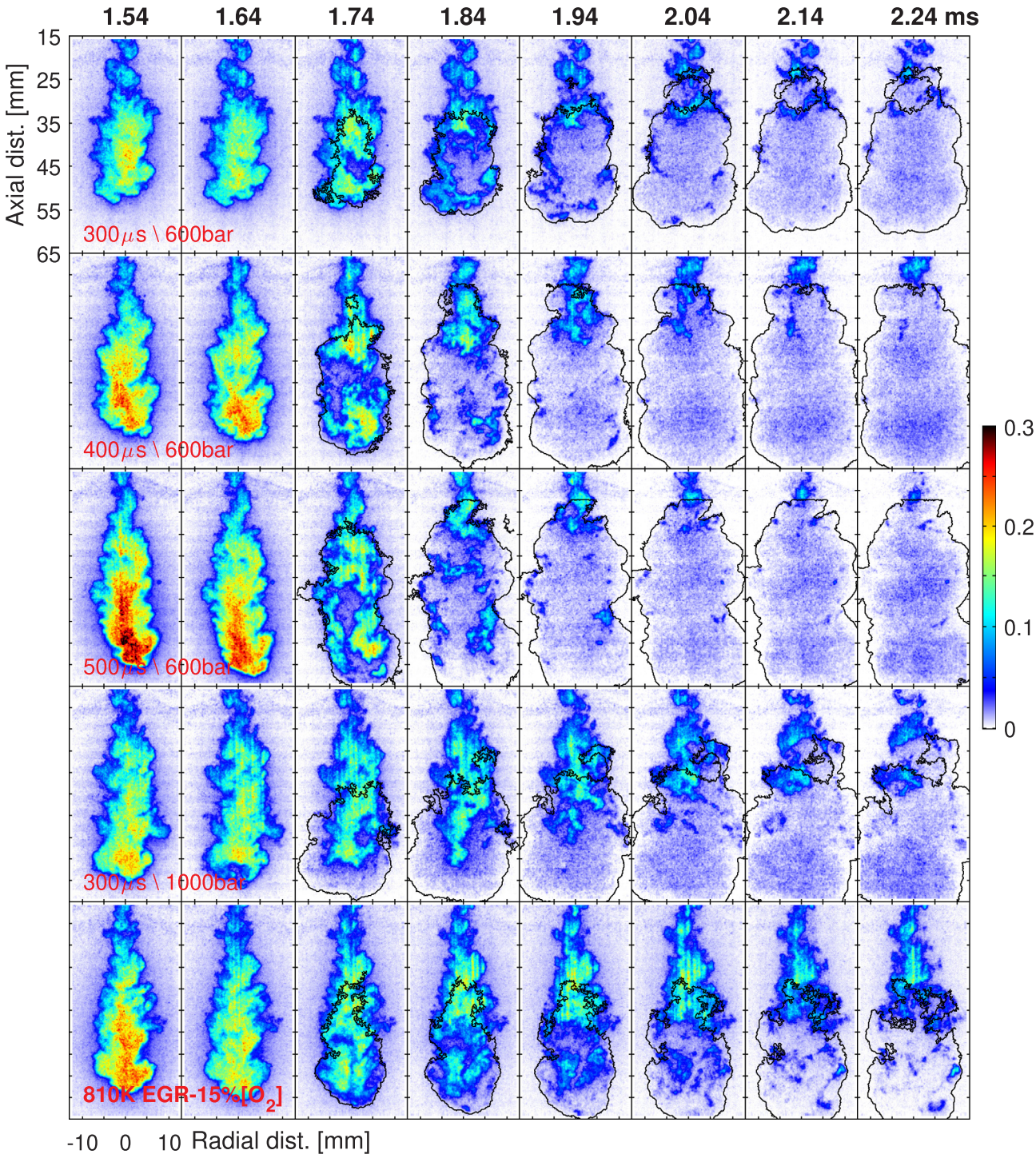

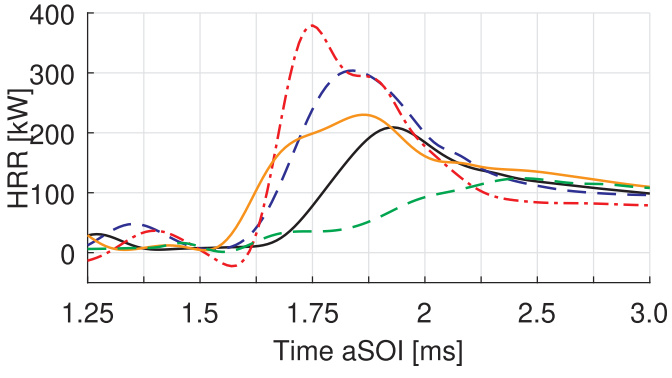

Line Style	Injection	Low-T ID	High-T ID
———	300μs \ 600bar	1.14 ms	1.62 ms
– – –	400μs \ 600bar	1.14 ms	1.60 ms
-·-·-	500μs \ 600bar	1.24 ms	1.65 ms
———	300μs \ 1000bar	1.04 ms	1.52 ms
– – –	810K EGR-15%[O_2]	0.94 ms	1.67 ms

(caption on next page)

Fig. 7. Dual-fuel (ϕ_{CH4} = 0.59) cases CH_2O-PLIF time-series for the variations of pilot injection parameters: ET variation (rows 1–3), p_{inj} variation (row 4) and [O_2] variation (row 5, ET = 400 µs, p_{inj} = 600 bar). The same color scale was used for all CH_2O-PLIF panel within this work. Simultaneously acquired Schlieren contours are superimposed on panels after the ID (black line). The bottom plot shows the HRR for all five cases, and the table states the low-T and high-T ID. T_{SOI} = 770 K (except 15% [O_2] case, row 5).

and dual-fuel case is detected in the 15% [O_2] case (5th row of Fig. 7). The Part 1 of this work [54] reported that the combination of CH_4 and reduced [O_2] leads to a reduced HRR rise and a low peak-HRR. This is well visible both in the HRR and in the CH_2O-consumption comparison of the 15% [O_2] case to the 21% [O_2] cases. In the 15% [O_2] case, a slow disappearance of CH_2O is already visible at 1.64 ms over the large portions of the spray head with a large PLIF signal. This is also in-line with a small rise of HRR at that time. However, the CH_2O disappears very slowly, and even in the head of the spray, a considerable amount of CH_2O persists for more than 0.5 ms after ignition. In the wake of the spray, CH_2O remains unburnt even longer. This is contrary to the diesel-case, where no considerable influence of reduced [O_2] on the lean CH_2O persistence was observed. The decreased flame speed (see Fig. 4) combined with the amplified spatial ignition-time stratification explains this observation.

3.3. Flame-contour spreading rate

Imaging of the CH_2O-PLIF provides very high-fidelity images at a somewhat limited frame rate. In the diesel-cases, even at T_{SOI} = 770 K, most of the pilot-fuel is consumed within just 2–3 image frames (200–300 µs). However, this information is complemented by the line-of-sight information of the flame extent by OH* imaging at 40 kHz frame rate. Fig. 8 presents the evolution of flame-contour, detected by the OH* imaging for the diesel combustion events presented in Fig. 6. Nine time-instants from ignition until 0.2 ms are presented. The same plotting approach is repeated for the dual-fuel cases from Fig. 7, presented in Fig. 9.

All cases (diesel and dual-fuel at 21% [O_2], panels 1–4) initially show small ignition kernel(s) (red), which spread rapidly and merge into a larger kernel. In the diesel cases, the fast kernel spreading rate lasts for only about 100 µs, after which a slower spreading of the contour at around the spray tip and towards the injector is visible. Similarly, the dual-fuel cases initially show a fast initial kernel spreading rate. However, the maximal spreading rate is lower (contours closer together) and persists for a longer time. It takes 200–300 µs until a steady propagating contour is visible. As expected, the location and the spreading rate of OH* contours correspond well to the zones with consumed CH_2O from Figs. 6 and 7.

The evolution of the reduced [O_2] cases (5th panel, Figs. 8 and 9) shows somewhat “noisy” contours. This is because of an order of magnitude lower OH* signal at 15% [O_2] relative to 21% [O_2], resulting in a worsened signal to noise ratio. Despite the worse image quality, a very slow spreading of the contour from the first kernel appearance up to late in the combustion cycle is visible, in accordance with the CH_2O imaging and the HRR analysis. Corroborating with the CH_2O-PLIF information (Figs. 6 and 7), it seems that the CH_2O persists distributed throughout the spray tip while a premixed flame propagation might have already established at the spray tip much before all pilot fuel is consumed. Therefore, the observed contour expansion might be a combined effect of the pilot-fuel consumption within the jet as well as the flame propagation at the edges of the contour.

To provide a direct comparison, the spreading rate of flame kernels is quantified and averaged over 10 experimental repetitions. The contours from the schlieren images are used since in the cases with reduced [O_2] the weak OH* signal leads to poorly defined contours. Fig. 10 presents the expansion speed of schlieren contours for 1 ms after the autoignition for a variation of the T_{SOI}, ϕ_{CH4}, [O_2] as well as the injection parameters. This spreading rate is determined as the rate of change of the contour surface divided by the circumference of the contour.

At ϕ_{CH4} = 0, for all cases, very high peak spreading rates in the order of 40–50 m/s are detected, nevertheless, persisting for only about 100 µs (Fig. 10). In agreement with OH* contours (Fig. 9), the peak spreading rate of the dual-fuel cases is lower at 20–30 m/s. After the peak HRR, a steady spreading rate at around 1 m/s for diesel and 3 m/s for ϕ_{CH4} = 0.59 is established. In the diesel-case, the persistent contour expansion was attributed to the continued air entrainment and spray penetration. The difference between the steady spreading rate of the diesel and the dual-fuel cases is about twice the laminar flame speed (about 1 m/s, Fig. 4). This can be attributed to the corrugated flame surface induced by the spray. It is worth noticing that the kernel spreading rate becomes comparable to the predicted laminar flame speeds already 0.3–0.5 ms after ignition. The time instant, when the spreading rate stabilizes, could be interpreted as the end of the combustion transition phase. It is reasonable to assume that at this point the pilot-fuel does not anymore influence the premixed fuel combustion. However, due to the unknown morphology of the initiated flame surface, such analysis bears an inherent uncertainty and is therefore not attempted.

The influence of the charge and the pilot injection conditions on the spreading rate is investigated on the subplots of Fig. 10. First, a variation of T_{SOI} at ϕ_{CH4} = 0 and 0.59 is investigated on Fig. 10a. Independent of the T_{SOI}, the diesel cases show a high peak spreading rate followed by a rapid drop, in agreement with the very short pilot-fuel combustion duration under these conditions. In the dual-fuel cases, a decrease in the peak spreading rate with a decreasing T_{SOI} was measured. This is in agreement with the predicted higher ignition-time gradients in leaner mixtures at ignition (Fig. 3).

Extending this investigation to the variation of ET and p_{inj}, Fig. 10b

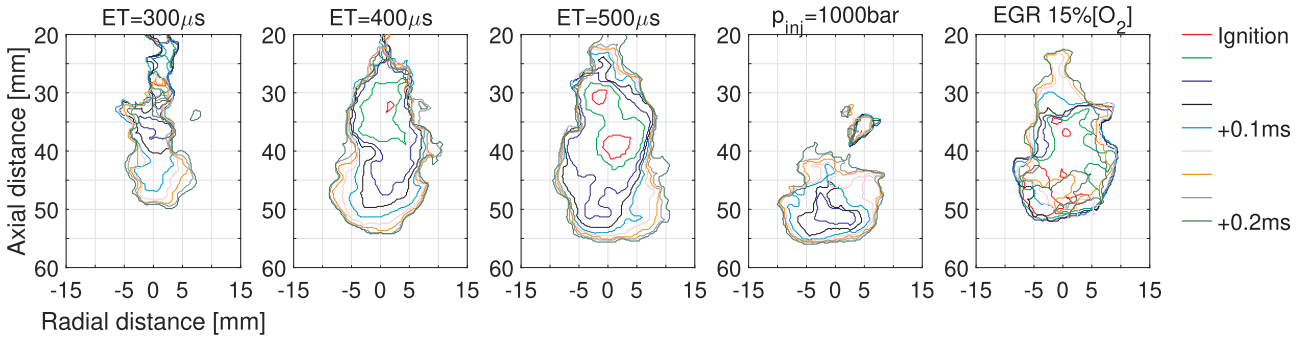

Fig. 8. Diesel case single-shot evolution of the OH* imaging based burnt zone contour. The time separation between contours is 25 µs. T_{SOI} = 770 K. The same combustion events as in Fig. 6 are presented.

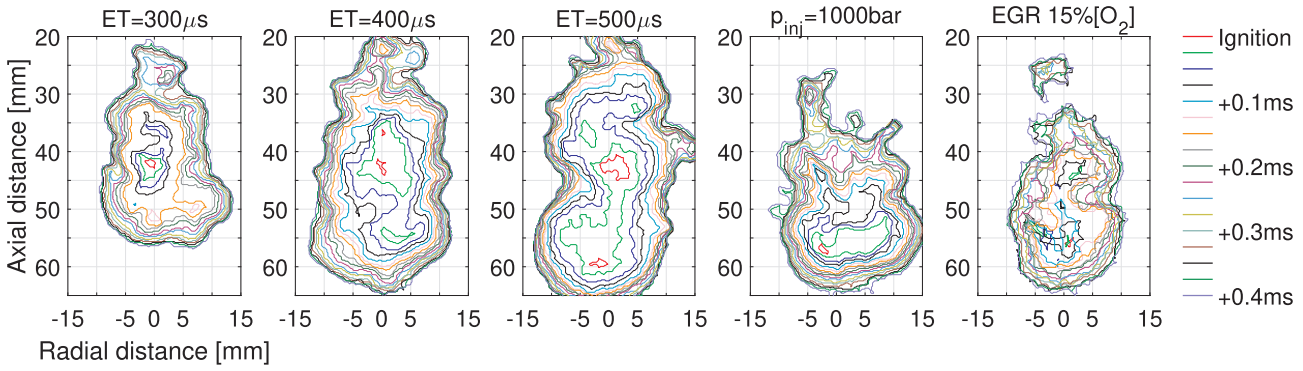

Fig. 9. Dual-fuel case (ϕ_{CH4} = 0.59) single-shot evolution of the OH* imaging based burnt zone contour. The time separation between contours is 25 μs. T_{SOI} = 770 K. The same combustion events as in Fig. 7 are presented.

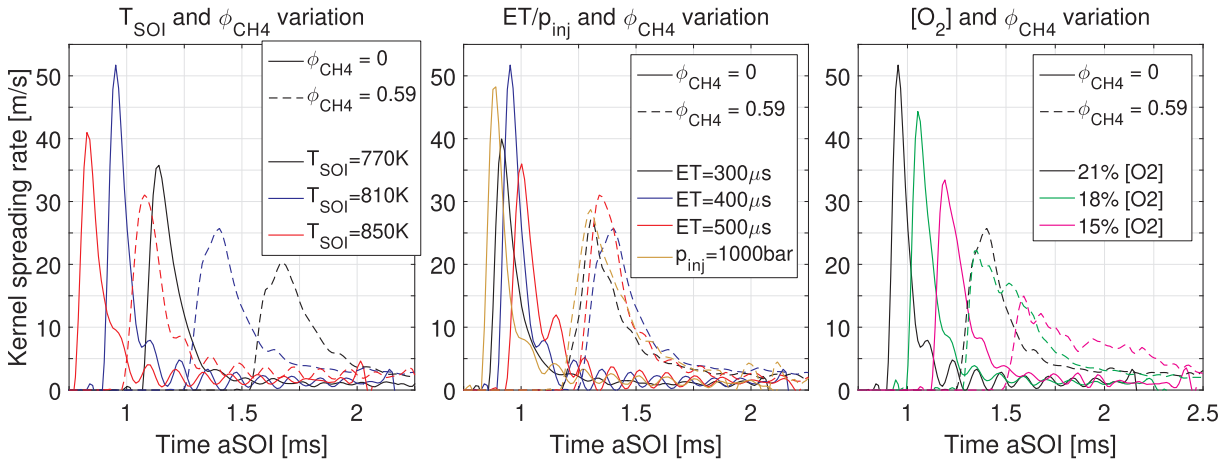

Fig. 10. Schlieren-based evolution of the kernel spreading-rate: (a) ϕ_{CH4} and T_{SOI} variation, (b) injection ϕ_{CH4} and ET or p_{inj} variation at T_{SOI} = 810 K, and (c) ϕ_{CH4} and [O_2] variation.

presents the kernel spreading rate for the ϕ_{CH4} = 0 and 0.59 cases at T_{SOI} = 810 K. No explicit dependence of the kernel expansion speed on injection parameters is visible, neither in the diesel nor in the dual-fuel case. This is also in line with the very similar pilot-fuel burning times detected at this T_{SOI} for all variations (Part 1 of this work [54]), attributed to the conditions believed to be far from the lean-out.

Finally, the influence of reduced [O_2] content on the kernel spreading rate at T_{SOI} = 810 K is studied (Fig. 10c). The influence of reduced [O_2] in the diesel case is moderate – a 35% reduction of the peak spreading rate and a prolonged pilot-fuel burning was detected. At 15% [O_2], a comparable peak speed and combustion time as for the T_{SOI} = 770 K (Fig. 10a) was measured. This is in agreement with the predicted higher spatial gradients of ignition-time due to the overall leaner conditions at ignition (Fig. 3). On the other hand, in the dual-fuel case, the ignition delay and the peak spreading rate appear to be decoupled, as already observed for the pilot-fuel combustion duration in Part 1 of this work. A slow and prolonged expansion of the kernel was observed. The ignition-time stratification due to the methane is not sufficient to alone explain this observation. Only a combination of this effect with the reduced flame-speed at lower [O_2] can explain this observation.

4. Discussion

The experimental results show a lower CH_2O persistence in the dual-fuel cases, and soon after ignition, the flame spreading rate becomes comparable to the laminar flame speed. This finding, in combination with the observation that in the cases with reduced [O_2] the burnt-zones spreading rate becomes very low, indicates the flame propagation is in some cases the faster combustion spreading mechanism in comparison to the auto-ignition front propagation. This effect occurs much before the complete pilot-fuel is consumed, which is an important indication for the dual-fuel combustion modeling – especially in the hybrid approaches coupling an auto-ignition submodel with a flame-propagation model. It is important that the submodel predicting the higher source terms, like implemented in [27,28], is used. The simpler approaches switching to the flame propagation immediately after ignition, or the approaches coupling the models based on the pilot-fuel mixture fraction, might predict non-physical solutions.

Nevertheless, another mechanism might importantly contribute to the overall combustion spreading rate: the number and the distribution of ignition kernels. With an increased number of auto-ignition kernels, the generated surface for the flame-propagation mechanism is enlarged. The evolution of the OH* contours (Figs. 8 and 9) shows several independent auto-ignition kernels to occur during ignition. Especially in the short injection cases (1st and 4th panels), several spatially separated ignition kernels are visible, which later merge into a single burnt zone. This considerably contributes to the overall burnt zone spreading in the initial combustion stages. Contrary, the longer injections (2nd and 3rd panels) with a faster initial contour spreading show a lower number of ignition kernels.

The correlation of the ignition kernels to the other combustion parameters is investigated to better understand the role of ignition kernels in the transition process. The ignition kernel appearance is detected based on the OH* imaging using a thresholding approach: If intensity in an area on the image exceeds the threshold, this indicates the appearance of a new kernel, except if on the preceding image at the

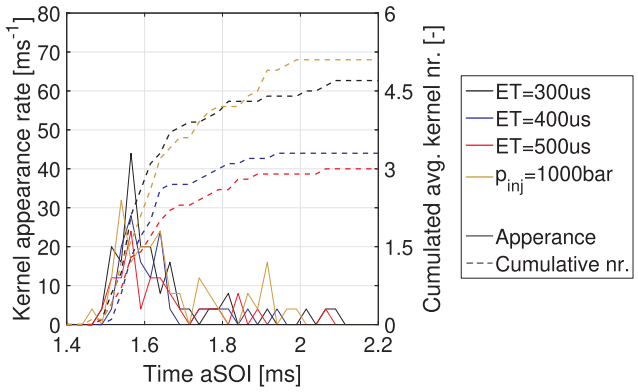

Fig. 11. OH* based ensemble-averaged ignition kernel appearance rate and ensemble-averaged cumulated ignition kernels number for a variation of ET and p_{inj}. Conditions: T_{SOI} = 770 K, ϕ_{CH4} = 0.59.

same location a kernel has already been detected. Therefore, the kernels formed by merging of two or more existing kernels are not counted as new. Fig. 11 presents the ensemble averaged rate of new kernel appearance and cumulated kernel number for the varied injection ET and p_{inj} under the dual-fuel conditions of Figs. 7 and 9 (T_{SOI} = 770 K, ϕ_{CH4} = 0.59).

Most of the ignition kernels for all cases appear during the rapid consumption of CH_2O within 0.2 ms after ignition (Fig. 11). All injections show a high kernel appearance rate during this time. Due to only 10 experimental repetitions and a high image frame rate, the appearance rate is noisy late after ignition. Nevertheless, a tail of the appearance rate is visible. It corresponds well to the time when new kernels appear in the wake of the spray and consume the remaining CH_2O (Figs. 7 and 9). The high-pressure injection, with the longest persistence of CH_2O in the wake of the jet, shows a largest number of the late-appearing ignition kernels.

The total number of detected ignition kernels correlates well both to the decreasing injection duration and to the higher p_{inj}. Therefore, the total number of ignition kernels appears to be inversely proportional to the mean pilot-fuel equivalence ratio (ϕ_{C12H26}) at ignition. This indicates that many ignition kernels appear in the late stages of combustion, when pilot-fuel combustion is in general slow. In those cases, small fluctuations in the mixture autoignition time lead to new autoignitions kernels. This is important, since it indicates that in many cases, the flame propagation is too slow to consume the very lean mixtures in the wake of the pilot-spray and indicates a substantial role of autoignition also in the late stages of pilot-jet combustion. To confirm this statement, Fig. 12 investigates the correlations of the number of ignition kernel number to the parameters relevant for the fuel stratification and lean-out: ID, pilot-fuel spray volume at ignition, and pilot combustion duration (t_v).

A positive correlation of the ignition kernel number to a longer ignition delay, a larger spray volume at ignition, and to a longer pilot-fuel combustion duration is seen on Fig. 12. No clear influence of methane on the number of ignition kernels is evident, except for its deferring effect on ignition. Overall, these observations lead to a conclusion, that the conditions unfavorable for ignition (long ignition delays, less reactive mixture at ignition) lead to more distributed reactive zones and slow pilot-fuel combustion. This has a consequence of multiple ignition spots at the locally most reactive mixture. The naïve but intuitive assumption, that more ignition kernels would initiate a larger flame surface within the pilot-fuel jet and therefore result in a faster pilot-fuel combustion than in cases with less kernels, proves wrong in this case.

Additional confirmation of this conclusion can be gained by comparing the correlation of kernel number to the ID and the spray volume for different injections (Fig. 12 left, middle). The shorter injections show a higher number of ignition kernels at the same ID (Fig. 12 left), or at the same spray volume (Fig. 12 middle). This clearly shows that leaner conditions at ignition lead to a larger number of ignition kernels, resulting from the large lean regions upstream of the spray tip.

5. Future work

The investigations revealed a complex interplay of the methane influence on the ignition delay stratification and on the turbulent flame speeds. Several consistent indications of both autoignition and turbulent mixing playing a significant role in the transition from ignition to the premixed flame propagation clearly motivate further investigations of the topic: high-fidelity CRFD investigations in LES or DNS context could be used to elucidate the relative contributions of both kernel expansion mechanisms and extend the conclusions of this work. On the experimental side, use of other gaseous fuels than methane could elucidate the role of premixed-fuel in the combustion transition – by using ethane instead of methane, the role of the chemical influence of methane could be highlighted. Ethane has a similar laminar flame speed but is expected to have a lower impact on the ignition delay. On the other hand, by using hydrogen instead of methane, the role of the flame-propagation can be stressed due to the increased laminar flame speed of hydrogen. Finally, with a forced ignition (laser-plasma) within the pilot-fuel plume prior to the autoignition, the turbulent flame speeds in the spray could be assessed. A comparison of the forced ignition kernel to the auto-igniting kernel expansion speed would then offer a further insight into the transition process.

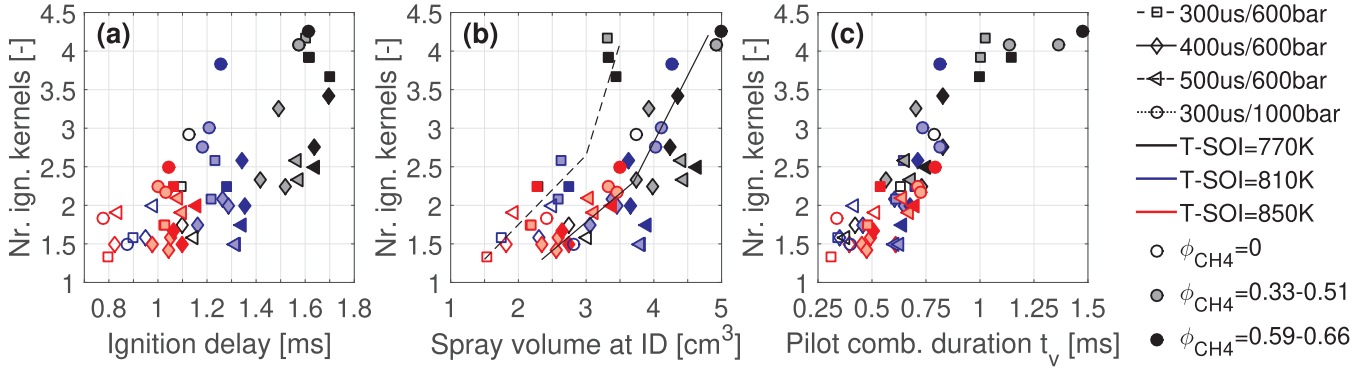

Fig. 12. Correlation of ignition kernel number to (a) the ignition delay, (b) to the spray volume at ignition, and (c) to the pilot-fuel combustion duration t_v. Marker shape indicates the pilot injection parameters, marker color the T_{SOI} and marker fill the ϕ_{CH4}, according to the legend. The added lines shall help the reader to orient on the plot.

6. Conclusions

The underlying processes governing the pilot-fuel burning during the transition from ignition to premixed flame propagation in dual-fuel engines is investigated in a rapid compression expansion machine. Simultaneous high-speed CH_2O-PLIF, Schlieren, and OH* chemiluminescence imaging is used to detect the pilot-fuel first-stage combustion products, ignition delay, and locations as well as the spreading rate of the ignition kernels. An extensive matrix of measurements with a variation of T_{SOI}, ϕ_{CH4}, pilot injector ET, and p_{inj} as well as a variation of charge oxygen content [O_2] is presented. Experimental investigations are corroborated with numerical calculations using homogeneous reactor and laminar flame speed simulations for different methane/dodecane/air mixtures. The investigations focus on determining the role of (a) ignition kernel number, (b) ignition delay stratification due to the chemical influence of methane and (c) the role of turbulent flame propagation during the pilot-fuel burning. The correlations of various parameters are investigated and the measured values compared to the simulation predictions.

Based on the analysis of experimental and numerical results the following conclusions can be drawn:

1. A good agreement of the CH_2O formation (cool flames) and consumption rate (high-T burning) with the HRR is reported. This gives additional confidence in the interpretation of HRR data presented in Part 1 of this work.
2. At low T_{SOI}, the ignition occurs in the fuel-richest mixture available in the fuel-jet. Furthermore, when the dwell time between the EOI and ignition becomes large, the fuel-jet is torn into several regions along the spray axis, resulting in multiple ignition locations. After the rapid combustion onset, the persisting CH_2O indicating unburnt pilot-fuel is found mostly in the wake of the jet as well as in the very lean regions at the jet boundary.
3. Homogeneous reactor (HR) calculations indicate a considerable sensitivity of the lean pilot-fuel mixture ignition delay to the pilot-fuel equivalence ratio. This effect is amplified under a reduced T_{SOI}. This explains the observed moderate prolongation of the pilot-fuel burning time t_v under the dual-fuel conditions. The effect is further pronounced under reduced [O_2] conditions. Nevertheless, this additional ignition-time stratification is insufficient to solely explain the strongly prolonged pilot-fuel combustion duration at reduced [O_2] conditions.
4. In the dual-fuel mixtures, where the HR calculations showed a high ignition time stratification ($\phi_{C12H26} < 0.5$), flame speeds of up to 3 m/s were predicted. Under reduced [O_2] conditions at the same concentration of pilot-fuel, the laminar flame speeds are more than 50% lower. This explains the strongly prolonged pilot-fuel combustion duration in the dual-fuel cases with a lower [O_2]. A firm reliance of the transition process on the turbulent flame propagation through the pilot-fuel jet is indicated by this finding.
5. The maximal kernel expansion speed decreases at higher ϕ_{CH4}, consistently with the observed prolonged pilot combustion duration. After ignition, the kernel expansion speed quickly drops to values comparable to the laminar flame speeds of dodecane/methane/air mixtures. This indicates that the turbulent flame propagation mechanism might considerably contribute to the overall pilot-fuel consumption, even before a flame propagation in the methane/air surrounding is established.
6. A strong indication of the flame propagation during the pilot-fuel consumption is given by the CH_2O persistence late after ignition. HR calculations predict a long persistence of CH_2O in the dual-fuel cases, contrary to the experimental observation. This indicates that in the dual-fuel cases a considerable portion of the lean pilot-fuel mixtures is burnt through the flame propagation mechanism.
7. At ignition and during the fast initial HRR, the flame kernels spread through the mechanism of auto-igniting front spreading alongside with the appearance of several new autoignition kernels. The overall number of ignition kernels increases under conditions with a prolonged ID and a longer dwell time. Methane was found to have no influence on the ignition kernel number beside it's deferring effect on the autoignition. A strong correlation between a higher kernel number and a longer pilot-fuel burning indicates that a higher number of ignition kernels occurs under the conditions not favorable for rapid spreading of the auto-igniting front.

Overall, the findings give a detailed understanding of the involved processes in the dual-fuel combustion during the transition from pilot-fuel auto-ignition into premixed flame initiation. The comprehensive study provides essential information facilitating the further development of dual-fuel combustion modeling approaches with respect to the transition characteristics and dominant propagation mechanism. Subsequently, improved and adequate simulation methodologies can be elaborated to provide operational parameters for an optimum efficiency-emission trade-off in dual-fuel engines.

Acknowledgements

Financial support from the Competence Center for Energy and Mobility (CCEM, project "ScheDual") and the Swiss Federal Office of Energy (grants SI/501123-01 and SI/501584-01) is gratefully acknowledged. This study has benefited from discussions in the Technology Collaboration Programme "clean and efficient combustion" of the International Energy Agency.

References

[1] Zhou L, Liu Y-F, Wu C-B, Sun L, et al. Effect of the diesel injection timing and the pilot quantity on the combustion characteristics and the fine-particle emissions in a micro-diesel pilot-ignited natural-gas engine. Proc Instit Mech Eng, Part D 2013;227(8):1142–52. https://doi.org/10.1177/0954407013480452.
[2] Papagiannakis RG, Hountalas DT. Combustion and exhaust emission characteristics of a dual fuel compression ignition engine operated with pilot diesel fuel and natural gas. Energy Convers Manage 2004;45(18):2971–87. https://doi.org/10.1016/j.enconman.2004.01.013.
[3] Wei L, Geng P. A review on natural gas/diesel dual fuel combustion, emissions and performance. Fuel Process Technol 2016;142(Supplement C):264–78. https://doi.org/10.1016/j.fuproc.2015.09.018.
[4] Rochussen J, Yeo J, Kirchen P. Effect of fueling control parameters on combustion and emissions characteristics of diesel-ignited methane dual-fuel combustion; 2016, SAE Technical Paper 2016-01-0792. https://doi.org/10.4271/2016-01-0792.
[5] Liu J, Yang F, Wang H, Ouyang M, et al. Effects of pilot fuel quantity on the emissions characteristics of a Cng/diesel dual fuel engine with optimized pilot injection timing. Appl Energy 2013;110(Supplement C):201–6. https://doi.org/10.1016/j.apenergy.2013.03.024.
[6] Magno A, Mancaruso E, Vaglieco BM. Combustion analysis of dual fuel operation in single cylinder research engine fuelled with methane and diesel; 2015. SAE Technical Paper 2015-24-2461. https://doi.org/10.4271/2015-24-2461.
[7] Papagiannakis RG, Hountalas DT. Experimental investigation concerning the effect of natural gas percentage on performance and emissions of a di dual fuel diesel engine. Appl Therm Eng 2003;23(3):353–65. https://doi.org/10.1016/S1359-4311(02)00187-4.
[8] Schlatter S, Schneider B, Wright Y, Boulouchos K. Experimental study of ignition and combustion characteristics of a diesel pilot spray in a lean premixed methane/air charge using a rapid compression expansion machine. SAE Technical Paper 2012-01-0825; 2012. https://doi.org/10.4271/2012-01-0825.
[9] Schlatter S, Schneider B, Wright YM, Boulouchos K. N-heptane micro pilot assisted methane combustion in a rapid compression expansion machine. Fuel 2016;179:339–52. https://doi.org/10.1016/j.fuel.2016.03.006.
[10] Ahmad Z, Aryal J, Ranta O, Kaario O, et al. An optical characterization of dual-fuel combustion in a heavy-duty diesel engine. SAE Technical Paper 2018-01-0252; 2018. https://doi.org/10.4271/2018-01-0252.
[11] Rochussen J, Kirchen P. Characterization of reaction zone growth in an optically accessible heavy-duty diesel/methane dual-fuel engine. Int J Engine Res 2019;20(5):483–500. https://doi.org/10.1177/1468087418756538.
[12] Dronniou N, Kashdan J, Lecointe B, Sauve K, et al. Optical investigation of dual-fuel Cng/diesel combustion strategies to reduce Co_2 emissions. SAE Int J Engines 2014;7:873–87. https://doi.org/10.4271/2014-01-1313.
[13] Srna A, Bruneaux G, von Rotz B, Bombach R, et al. Optical investigation of sooting propensity of N-dodecane pilot/lean-premixed methane dual-fuel combustion in a rapid compression-expansion machine. SAE Technical Paper 2018-01-0258; 2018. https://doi.org/10.4271/2018-01-0258.
[14] Srna A, Bolla M, Wright YM, Herrmann K, et al. Effect of methane on pilot-fuel auto-

ignition in dual-fuel engines. Proc Combus Instit 2018;37. https://doi.org/10.1016/j.proci.2018.06.177.
[15] Srna A, Barro C, Herrmann K, Möri F, et al. POMDME as an alternative pilot fuel for dual-fuel engines: optical study in a Rcem and application in an automotive size dual-fuel diesel engine. SAE Technical Paper 2018-01-1734; 2018. https://doi.org/10.4271/2018-01-1734.
[16] Kahila H, Wehrfritz A, Kaario O, Vuorinen V. Large-Eddy simulation of dual-fuel ignition: diesel spray injection into a lean methane-air mixture. Combust Flame 2019;199:131–51. https://doi.org/10.1016/j.combustflame.2018.10.014.
[17] Abd Alla GH, Soliman HA, Badr OA, Abd Rabbo MF. Effect of pilot fuel quantity on the performance of a dual fuel engine. Energy Convers Manage 2000;41(6):559–72. https://doi.org/10.1016/S0196-8904(99)00124-7.
[18] Abdelaal MM, Hegab AH. Combustion and emission characteristics of a natural gas-fueled diesel engine with Egr. Energy Convers Manage 2012;64:301–12. https://doi.org/10.1016/j.enconman.2012.05.021.
[19] Nithyanandan K, Gao Y, Wu H, Lee C-F, et al. An optical investigation of multiple diesel injections in Cng/diesel dual-fuel combustion in a light duty optical diesel engine; 2017, SAE Technical Paper 2017-01-0755. https://doi.org/10.4271/2017-01-0755.
[20] Barro C, Nani C, Hutter R, Boulouchos K. Spray model based phenomenological combustion description and experimental validation for a dual fuel engine, SAE Technical Paper 2017-24-009, doi: http://dx.doi.org/10.4271/2017-24-0098.
[21] Papagiannakis RG, Hountalas DT. Combustion and exhaust emission characteristics of a dual fuel compression ignition engine operated with pilot diesel fuel and natural gas. Energy Convers Manage 2004;45(18–19):2971–87. https://doi.org/10.1016/j.enconman.2004.01.013.
[22] Goyal H, Kook S, Ikeda Y. The influence of fuel ignition quality and first injection proportion on gasoline compression ignition (Gci) combustion in a small-bore engine. Fuel 2019;235:1207–15. https://doi.org/10.1016/j.fuel.2018.08.090.
[23] Vallinayagam R, An Y, Vedharaj S, Sim J, et al. Naphtha Vs. dieseline – the effect of fuel properties on combustion homogeneity in transition from Ci combustion towards Hcci. Fuel 2018;224:451–60. https://doi.org/10.1016/j.fuel.2018.03.123.
[24] Kokjohn SL, Musculus MPB, Reitz RD. Evaluating temperature and fuel stratification for heat-release rate control in a reactivity-controlled compression-ignition engine using optical diagnostics and chemical kinetics modeling. Combust Flame 2015;162(6):2729–42. https://doi.org/10.1016/j.combustflame.2015.04.009.
[25] Wissink ML, Curran SJ, Roberts G, Musculus MPB, et al. Isolating the effects of reactivity stratification in reactivity-controlled compression ignition with iso-octane and NI – heptane on a light-duty multi-cylinder engine. Int J Engine Res 2018;19(9). https://doi.org/10.1177/1468087417732898.
[26] Soriano BS, Richardson ES. Investigation of flame propagation in autoignitive blends of n-heptane and methane fuel. Combust Theor Model 2019. https://doi.org/10.1080/13647830.2019.1614228.
[27] Soriano BS, Richardson ES, Schlatter S, Wright YM. Conditional moment closure modelling for dual-fuel combustion engines with pilot-assisted compression ignition. SAE Technical Paper 2017-01-2188; 2017. https://doi.org/10.4271/2017-01-2188.
[28] Seddik O, Pandurangi S, Bolla M, Boulouchos K, et al., Flamelet generated manifolds applied to dual-fuel combustion of lean methane/air mixtures at engine relevant conditions ignited by N dodecane micro pilot sprays. SAE Technical Paper 2019-01-1163, https://doi.org/10.4271/2019-01-1163.
[29] Kammermann T, Koch J, Wright YM, Soltic P, et al. Generation of turbulence in a Rcem towards engine relevant conditions for premixed combustion based on Cfd and Piv investigations. SAE Int J Engines 2017;10(4). https://doi.org/10.4271/2017-24-0043.
[30] Bakker PC, Maes N, Dam N. The potential of on- and off-resonant formaldehyde imaging combined with bootstrapping in diesel sprays. Combust Flame 2017;182:20–7. https://doi.org/10.1016/j.combustflame.2017.03.032.
[31] Skeen SA, Manin J, Pickett LM. Simultaneous formaldehyde Plif and high-speed schlieren imaging for ignition visualization in high-pressure spray flames. Proc Comb Inst 2015;35:3167–74. https://doi.org/10.1016/j.proci.2014.06.040.
[32] Lachaux T, Musculus MPB. In-cylinder unburned hydrocarbon visualization during low-temperature compression-ignition engine combustion using formaldehyde Plif. Proc Comb Inst 2007;31:2921–9. https://doi.org/10.1016/j.proci.2006.07.044.
[33] Srna A, Bruneaux G, von Rotz B, Bombach R, et al. Optical investigation of sooting propensity of N-dodecane pilot/lean-premixed methane dual-fuel combustion in a rapid compression-expansion machine; 2018. SAE Technical Paper 2018-01-0258. https://doi.org/10.4271/2018-01-0258.
[34] O'Connor J, Musculus M. Optical investigation of the reduction of unburned hydrocarbons using close-coupled post injections at Ltc conditions in a heavy-duty diesel engine. SAE Int J Engines 2013;6(1):379–99. https://doi.org/10.4271/2013-01-0910.
[35] Collin R, Nygren J, Richter M, Aldén M, et al. Simultaneous oh-and formaldehyde-Lif measurements in an Hcci engine. SAE Technical paper 2003-01-3218; 2003. https://doi.org/10.4271/2003-01-3218.
[36] Skeen S, Manin J, Pickett LM. Visualization of ignition processes in high-pressure sprays with multiple injections of N-dodecane. SAE Int J Engines 2015;8:696–715. https://doi.org/10.4271/2015-01-0799.
[37] Salaun E, Apeloig J, Grisch F, Yvonnet C-E, et al. Optical investigation of ignition timing and equivalence ratio in dual-fuel Cng/diesel combustion; 2016. SAE Technical Paper 2016-01-0772. https://doi.org/10.4271/2016-01-0772.
[38] Srna A, Bombach R, Herrmann K, Bruneaux G. Characterization of the spectral signature of dual-fuel combustion luminosity: implications for evaluation of natural luminosity imaging. Appl Phys B 2019;125(7). https://doi.org/10.1007/s00340-019-7222-z.
[39] Najafabadi MI, Egelmeers L, Somers B, Deen N, et al. The influence of charge stratification on the spectral signature of partially premixed combustion in a light-duty optical engine. Appl Phys B 2017;123. https://doi.org/10.1007/s00340-017-6688-9.
[40] Pickett LM. Engine combustion network. http://www.sandia.gov/ecn/dieselSprayCombustion.php; 2013.
[41] Pickett LM. Engine Combustion Network Website. https://ecn.sandia.gov/diesel-spray-combustion/experimental-diagnostics/light-based-ignition-delay/2013; 2013 [11 May 2019].
[42] Yao MF, Zheng ZL, Liu HF. Progress and recent trends in homogeneous charge compression ignition (Hcci) engines. Prog Energy Combust Sci 2009;35(5):398–437. https://doi.org/10.1016/j.pecs.2009.05.001.
[43] Zeldovich YB. Regime classification of an exothermic reaction with nonuniform initial conditions. Combust Flame 1980;39(2):211–4. https://doi.org/10.1016/0010-2180(80)90017-6.
[44] Dahms RN, Paczko GNA, Skeen SA, Pickett LM. Understanding the ignition mechanism of high-pressure spray flames. Proc Comb Inst 2017;36:2615–23. https://doi.org/10.1016/j.proci.2016.08.023.
[45] Musculus MP, Lachaux T, Pickett LM, Idicheria CA. End-of-injection over-mixing and unburned hydrocarbon emissions in low-temperature-combustion diesel engines. SAE Technical Paper 2007-01-0907; 2007, https://doi.org/10.4271/2007-01-0907.
[46] Musculus MP, Kattke K. Entrainment waves in diesel jets. SAE Int J Engines 2009;2:1170–93. https://doi.org/10.4271/2009-01-1355.
[47] Blomberg CK, Zeugin L, Pandurangi SS, Bolla M, et al. Modeling split injections of Ecn "spray a" using a conditional moment closure combustion model with Rans and Les. SAE Int J Engines 2016;9. https://doi.org/10.4271/2016-01-2237.
[48] Ranzi E, Frassoldati A, Stagni A, Pelucchi M, et al. Reduced kinetic schemes of complex reaction systems: fossil and biomass-derived transportation fuels. Int J Chem Kinet 2014;46(9):512–42. https://doi.org/10.1002/kin.20867.
[49] Ghaderi Masouleh M, Wehrfritz A, Kaario O, Kahila H, et al. Comparative study on chemical kinetic schemes for dual-fuel combustion of N-dodecane/methane blends. Fuel 2017;191:62–76. https://doi.org/10.1016/j.fuel.2016.10.114.
[50] Ranzi E, Frassoldati A, Grana R, Cuoci A, et al. Hierarchical and comparative kinetic modeling of laminar flame speeds of hydrocarbon and oxygenated fuels. Prog Energy Combust Sci 2012;38(4):468–501. https://doi.org/10.1016/j.pecs.2012.03.004.
[51] Sarathy SM, Westbrook CK, Mehl M, Pitz WJ, et al. Comprehensive chemical kinetic modeling of the oxidation of 2-methylalkanes from C7 to C20. Combust Flame 2011;158:2338–57. https://doi.org/10.1016/j.combustflame.2011.05.007.
[52] Matalon M, Creta F. The "turbulent flame speed" of wrinkled premixed flames. Comptes Rendus Mécanique 2012;340(11):845–58. https://doi.org/10.1016/j.crme.2012.10.031.
[53] Grossmann F, Monkhouse PB, Ridder M, Sick V, et al. Temperature and pressure dependences of the laser-induced fluorescence of gas-phase acetone and 3-pentanone. Appl Phys B 1996;62:249–53.
[54] Srna A., von Rotz B, Herrmann K, Boulouchos K, Bruneaux G. Experimental investigation of pilot-fuel combustion in dual-fuel engines, Part 1: Thermodynamic analysis of combustion phenomena, Fuel, in press, https://doi.org/10.1016/j.fuel.2019.115642.